Tailoring the Rheology of Shear Thickening Fluids by Regulating the Particle Size of Dispersed Phase for Enhancing the Impact Resistance of Aramid Fabrics

Komal Talreja, Aranya Ghosh, Sanchi Arora, Abhijit Majumdar, and Bhupendra Singh Butola*

Department of Textile & Fibre Engineering, Indian Institute of Technology Delhi, New Delhi 110016, India
(Received February 12, 2021; Revised September 29, 2021; Accepted September 30, 2021)

Abstract: Rheological behaviour of shear thickening fluid (STF) is influenced by particle size, particle shape, concentration of particles etc. This study deals with the effect of particle size and its distribution on the rheological behaviour of STFs and ensuing impact resistance of Kevlar® fabrics treated with them. Synthesis of submicron sized silica particles of three different sizes was carried out by following the Stöber method. Corresponding STFs consisting of 67 % silica particles were prepared and their rheological behaviour was evaluated. Decrease in particle size coupled with particle size uniformity significantly contributes to enhancement in dilatancy of STFs. Further, Kevlar® fabric was impregnated with these STFs for assessing their impact resistance performance. Fabric impregnated with STF prepared from the finest and uniform silica particles, having the highest peak viscosity, exhibited the best impact resistance performance among all STF impregnated fabrics. These findings show that the particle size and its distribution decisively influence the thickening behaviour of STF which in turn plays a critical role in determining the impact energy absorption by high-performance fabrics.

Keywords: Impact energy, Polydispersity, Rheology, Shear thickening fluid, Stöber process

Introduction

Shear thickening fluid (STF) is a dense colloidal dispersion which shows reversible viscosity transition under applied shear stress [1]. It is prepared by mixing solid, hard submicron sized particles in a carrier fluid like polyethylene glycol, polypropylene glycol, glycerol, etc. It exhibits non-Newtonian flow behaviour under shear owing to the formation of hydroclusters which results in abrupt change in viscosity of the system. The unique attributes of STF make it eligible to be used in myriad applications like polishing of steel bars, enhancing performance of cutting tools, modifying vibration attenuation of sandwich structures or carbon fibre reinforced polymeric tubes for use in aerospace, automotive, sports and medical applications [2-5]. High-performance fabrics impregnated with STF exhibit improved resistance to impact due to unique thickening phenomenon of the latter [6-8]. The basic mechanism of impact resistance offered by STF impregnated fabric has for long been a matter of debate among the researchers. One group of researchers [9-11] believes that the pivotal role of STF is contributed by its inherent liquid to solid transition in presence of shear force which is triggered by the relative movement of yarns or filaments in the fabric during impact. Therefore, the formed hydroclusters (of solid particles) behave like a bonding material, engaging more secondary yarns. Hence, the entire fabric, and not only the impact zone, participates in the process of energy absorption. However, another group of researchers [12,13] claims that STF deposition in fabric increases inter-yarn friction, which ultimately results in higher yarn pull-out force, leading to increased impact energy absorption.

It is well established that physical and chemical parameters related to solid particles (dispersed phase of STF) such as roughness, hardness, surface chemistry, aspect ratio, size, size distribution and solid content significantly influence the rheological behaviour of an STF [14]. New contact rheology theory [15] reveals that particle size and size distribution are highly influential factors as they offer differing levels of contact friction for altering shear rheological performance of an STF. Barnes [16] reported that critical shear rate is inversely related to the square of particle radius at a fixed solid content condition. Using smaller diameter particles increases the number of particles (in unit volume) that exhibit stronger inter-particle forces which can be countered by higher shear force only. Therefore, the critical shear rate shifts to higher values. The reverse occurs while using larger diameter particles where less shear force is sufficient to overpower the inter-particle repulsive forces, resulting in lower values of critical shear rate. Similar findings have also been reported by several other researchers [17,18]. In the context of peak viscosity, Li *et al.* [18] found it to increase with decrease in size and size distribution of the particles; although some researchers [10, 19] contradict this statement on the basis of complete opposite observation. Another important decisive factor which can influence the rheology of an STF is particle size distribution. In this context, Barnes [16] observed that wider particle size distribution in the STF system did not improve shear thickening phenomenon, and rather proved detrimental. Wagstaff and Chaffey [20] observed similar findings and reported that blending of particles interrupted the formation of hydroclusters, resulting in a drastic decrease in peak viscosity.

Several researchers have also investigated the effect of particle size and its distribution on the impact energy

---

absorption of STF impregnated high-performance fabrics. Lee *et al*. [17] demonstrated a prominent influence of particle size of silica colloidal suspension on the inter-yarn frictional properties of the fabric treated with it, and subsequently on the ballistic resistance offered by the fabric. They observed that fabric impregnation with STF prepared from smaller particles led to huge increment in inter-yarn friction which resulted in significantly higher energy dissipation and less transverse deformation of fabric, and thus less blunt trauma. Very recently, Bajya *et al*. [21] carried out a similar study by developing 20-24 layered panels using Kevlar® fabrics impregnated with different STFs made from 500 nm and 100 nm powdered silica particles, and evaluated their ballistic resistance against small arms ammunition fired at 430±15 m s⁻¹. Contradictory to [17], they found larger particle based STF treated fabric panels to yield lower backface signature than that yielded by smaller particle based STF treated fabrics, despite more increase in inter-yarn friction in case of latter (similar to [17]). They attributed this discrepancy to lower critical shear rate as well as prolonged thickening of STF-500, thus indicating predominant contribution of shear thickening towards improvement in ballistic resistance, over contribution from increased inter-yarn friction. In yet another study aimed in similar direction, Mawkhlieng and Majumdar [10] performed a comparative analysis of impact energy absorption by Kevlar® fabrics impregnated with different monodispersed and bi-dispersed STFs composed of silica particles of three sizes, i.e. 100, 300 and 500 nm. Interestingly, they established the role of STF in enhancing impact energy absorption of Kevlar fabric irrespective of the value of inter-yarn friction. The fabrics impregnated with STF prepared using monodispersed silica particles of the highest diameter (500 nm) and having the highest peak viscosity, resulted in most superior impact resistance performance amongst all types of STF impregnated fabrics. Liu *et al*. [22] too highlighted the contribution of shear thickening phenomenon in impact energy absorption. Though the STF treated panels prepared by them using smaller silica particles (100 nm) exhibited 56 % increment in impact energy absorption owing to shear thickening, the larger silica particle (650 nm) based STF failed to contribute because the shear rate during impact surpassed its shear thickening rate range, due to which thickening could not occur.

The preceding discussion conjectures that the rheological characteristics of an STF play a major role in enhancing the impact resistance characteristics of treated fabrics [10,23, 24]. Hence, the current study aims to justify the effect of synthesising silica particles of different sizes with dominant polydispersity in terms of rheological behaviour of resultant STFs and impact resistance performance of fabrics impregnated with these STFs. Silica particles of three different submicron sizes were synthesised by Stöber

method, followed by preparation of corresponding STFs for rheological analysis. Further, the effect of these STFs on impact energy absorption of Kevlar® fabrics impregnated with them was studied.

Experimental

Materials

Precursor of silica particles, i.e. tetraethyl orthosilicate (TEOS), was procured from TCI Chemicals (India) Pvt. Ltd., India. Ethanol and ammonium hydroxide were supplied by Fisher Scientific, India. Polyethylene glycol (PEG) of molecular weight 200 g mol⁻¹ was acquired from MilliporeSigma, India. All the syntheses were carried out with deionised water. Commercially available ballistic grade *p*-aramid fabric (Kevlar® 802 F) was impregnated with different STFs. The fabric specifications are: areal density as 185±5 g m⁻², fabric sett (EPI×PPI, ends per inch×picks per inch) of 21×21 inch⁻², linear density of constituent yarns as 1000 denier. The procured Kevlar fabric with a coating of polytetrafluroethylene (PTFE) was used as received.

Synthesis of Silica Particles

Silica particles of different sizes were prepared by Stöber process [25]. The typical synthesis of silica nanoparticles was carried out as follows. An aqueous solution was prepared by mixing 1 M ammonium hydroxide in 89 m*l* ethanol. Water concentration was varied as 4, 6 and 8 M to obtain different sizes of particles. Simultaneously, another 1 M solution of TEOS was prepared in ethanol in a separate beaker. The latter solution was mixed with the former one (Figure 1) and stirred for 6 h at room temperature (30 °C). This mixture was centrifuged at 8000 rpm for 15 min and the formed silica particles were washed thrice with ethanol to
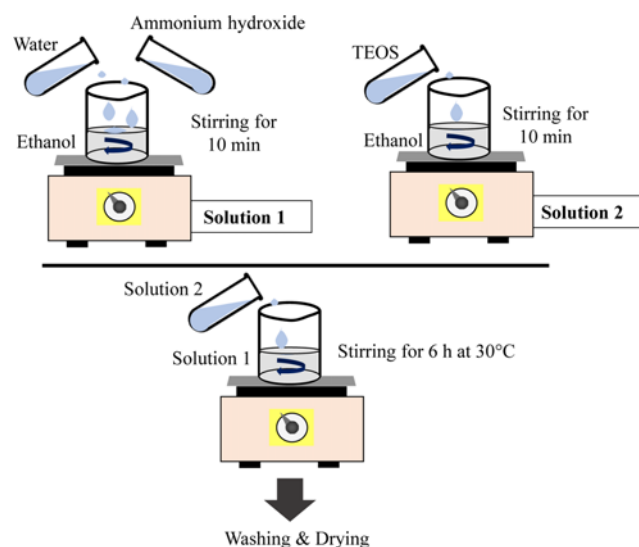

Figure 1. Schematic representation of synthesis of silica particles.
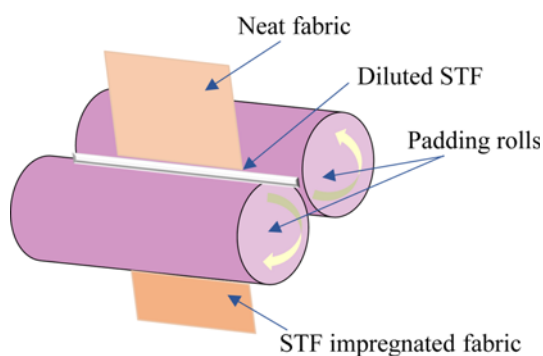
Figure 2. Impregnation of STF in Kevlar fabric using Lab Padder.

remove unreacted reagents. White silica powder was obtained by drying the washed particles in a vacuum oven at 70 °C for 1 h. Finally, the particles were again dried at 150 °C for 2 h to remove any traces of moisture. Using the described process, silica particles with three different particle sizes were synthesised by varying the concentration of water as 4, 6 and 8 M, and named as silica A, silica B and silica C, respectively.

Preparation of STF

The STFs of 67 % solid concentration (w/w) were prepared by dispersing silica particles in carrier fluid PEG 200. Firstly, silica particles were dispersed in ethanol using ultrasonicator (Elma S60 H, power: 550 W, frequency: 50-60 Hz) for 1 h at room temperature. Subsequently, PEG 200 was added to this mixture and sonication process was further continued for 4 h at 70 °C. Removal of ethanol during sonication was confirmed by repeatedly weighing the fluids. STFs prepared by silica A, B and C were named as STF A, STF B and STF C, respectively.

Impregnation of Kevlar Fabric with STF

Kevlar fabrics were impregnated with the prepared STFs on a horizontal Mathis Lab Padder as shown in Figure 2. Before impregnation, the dense STFs were diluted with ethanol at 1:4 w/v ratio and homogenised at 17,000 rpm for 10 min using OV5 Homogeniser. The impregnation process was carried out at 2 bar pressure and each fabric sample was dipped twice in diluted STF and squeezed through roller nip at a delivery speed of 3 m min^{-1}. At last, all impregnated fabrics were dried in a hot air oven at 80 °C for 45 min to evaporate residual ethanol.

Characterisation Techniques

Fourier Transform Infrared Spectroscopy (FTIR)

Formation of silica particles was confirmed using Perkin-Elmer Spectrum-BX FTIR instrument (ATR mode) in the wavenumber range of 4000-500 cm^{-1} by conducting 32 scans for each sample.

Scanning Electron Microscopy (SEM)

The shape and size of synthesised silica particles were analysed by SEM (Zeiss EVO 18). A thin coating of silica dispersion was drop-casted over a glass cover slip and dried at 70 °C for 4 h, and gold-coated before the testing.

Dynamic Light Scattering (DLS)

Size distribution of synthesised silica particles was investigated by Zetasizer Nano ZS90 using DLS principle. Dispersions of 0.1 g l^{-1} concentration were prepared for all particles using ethanol as diluent.

Rheological Analysis of STFs

Steady state rheological characterisation of prepared STFs was conducted using Anton Paar Physica MCR 51 stress-controlled rheometer. Parallel plate geometry having upper plate diameter as 25 mm was used. The gap between two plates was fixed at 0.5 mm. Rheological analysis was carried out over a wide range of shear rate, from 1 to 1500 s^{-1} at 25 °C.

Impact Testing

Impact resistance performance of neat and STF impregnated fabrics was evaluated by drop tower impact tester (CEAST, Model: Fractovis Plus), using ASTM D3763 method. A hemispherical indenter (diameter ~13 mm) attached with an external carriage mass of 19.97 kg was dropped at a speed of 4.5 m s^{-1} on clamped fabric sample of 160 mm×160 mm dimensions. The impact resistance of fabric samples was assessed in terms of peak energy, total energy absorption and force *vs* time behaviour. Average values of peak and total energy absorption corresponding to four specimens for each sample were calculated.

The areal density of STF impregnated fabrics is altered due to STF add-on. Thus, a normalising factor is necessary to compare the energy absorption of fabrics irrespective of their different areal densities. The normalised value of impact energy absorption was calculated by following equation (1),

$$E_n = \frac{E_a}{\left(1 + x/100\right)} \tag{1}$$

where E_n is the normalised energy absorption (J), E_a is the absolute energy absorption (J) and x is STF add-on (%), which is calculated using equation (2).

$$Add-on\,(\%) = \frac{Gain\ in\ fabric\ weight\ after\ STF\ impregnation}{Fabric\ weight\ before\ STF\ impregnation} \times 100 \tag{2}$$

Results and Discussion

Characterisation of Silica Particles

FTIR Analysis

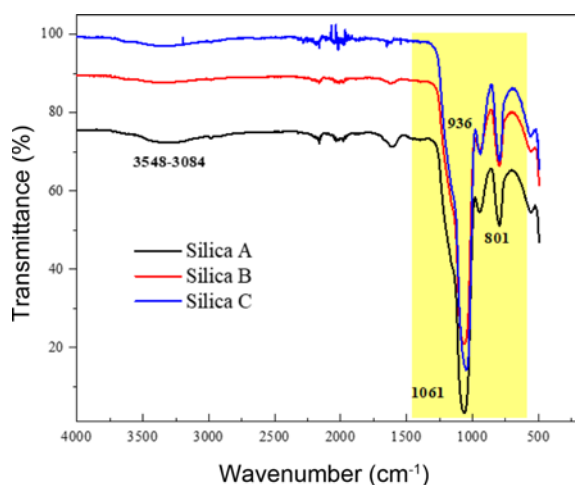Figure 3 depicts the FTIR spectra of different silica

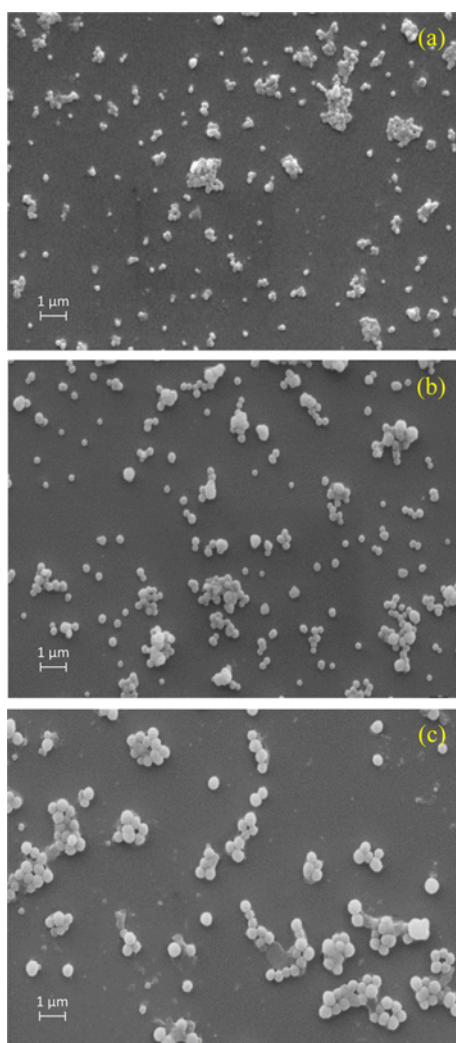**Figure 3.** FTIR spectra of synthesised silica particles.

Table 1. Mean diameter of various silica particles analysed from SEM micrographs

Particle type	Mean diameter (nm)	Standard deviation (nm)
Silica A	143.2	22.3
Silica B	244.3	33.9
Silica C	409.4	54.9

particles. It is observed that a strong band at 1061 cm^{-1} appears due to asymmetric vibration of Si-O-Si bonding of silica [26]. A weak band at 936 cm^{-1} is observed due to symmetric vibration of Si-OH (silanol) group. Furthermore, a bending vibration of Si-O group is found at 801 cm^{-1}. This confirms formation of silica particles. The broad band at 3084 to 3548 cm^{-1} is due to -OH bond, both from stretching vibration of Si-OH groups and adsorbed H$_2$O molecules over the silica surface [27].

SEM Analysis

Size and morphology of prepared silica particles as observed in SEM analysis are shown in Figure 4. As can be seen from the micrographs, the three silica particles are spherical in shape. The mean diameter corresponding to different particles were determined using ImageJ software (50 readings for each sample) and are presented in Table 1. It is evident that the size of silica particles gradually increases with increase in concentration of water from 4 M to 8 M. This finding suggests that higher amount of water augments hydrolysis of the precursor in basic medium [28] followed by higher rate of polycondensation of hydrolysed products, resulting in formation of larger silica particles.

Particle Size Analysis

Figure 5 presents the observations from DLS analysis of different silica particles. The results of particle size obtained
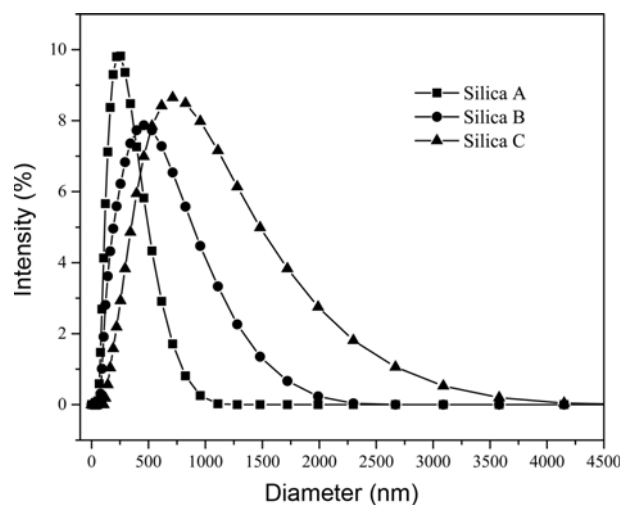

Figure 4. SEM micrographs of (a) silica A, (b) silica B, and (c) silica C particles.

Figure 5. Particle size distribution of different silica particles obtained from DLS analysis.

Table 2. Particle characteristics obtained from DLS analysis

Particle type	Z-average diameter (nm)	PDI
Silica A	214.7	0.22
Silica B	323.2	0.27
Silica C	584.5	0.32

from the DLS analysis follow a trend similar to as observed in SEM analysis. Thus, silica A has the smallest diameter of 215 nm, whereas silica B and C have diameters of 323 and 585 nm, respectively. The *Z-average* diameter of particle and polydispersity index (PDI) for each silica particle are presented in Table 2. As expected, the obtained mean diameter from DLS analysis is little higher than that calculated from SEM analysis. This is attributed to the fact that generally, in DLS mode, the hydrodynamic diameter of the particles is measured [29], which is higher than the actual size of the particles. Hence, in this study the mean diameters measured from SEM micrographs were considered for further analysis. Interestingly, silica A reveals a relatively narrow size distribution of diameter as compared to silica B and C. Polydispersity of the particles increases with increasing diameter of silica particles. Thus, the broadest size distribution is observed for silica C.

Rheological Analysis of Different STFs

Flow curves of various STFs are shown in Figure 6. Every curve exhibits three distinct zones, namely shear thinning, shear thickening and again shear thinning [30]. Initial shear thinning appears owing to alignment of particles along the direction of applied shear force, resulting in reduction in viscosity. This is followed by an abrupt increase in viscosity which is caused by formation of hydroclusters of particles. Finally, another thinning zone recurs just next to the
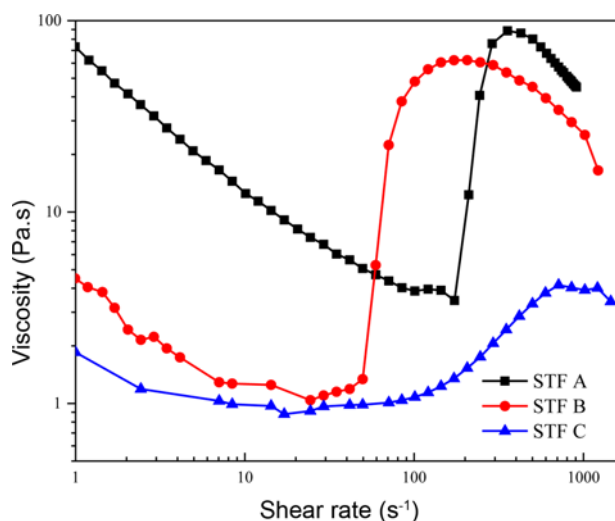
thickening zone owing to the destruction of formed metastable hydroclusters at higher shear rate [31]. On the other hand, relatively recent contact rheology model attributes particle to particle contact forces to be the major driving factor for shear thickening phenomenon [32,33]. At a certain shear force, particles in hydroclusters remove the thin layer of liquid medium (PEG) between them, resulting in physical contact with each other. Thus, a contact network structure is formed at high shear rate, which increases the viscosity of the system. In other words, hydrodynamic effect brings particles close to each other, initiating contact forces between them and consequently forming interlocked contact network structure. Here, STFs A and B exhibit discontinuous shear thickening (DST) phenomena whereas STF C shows continuous shear thickening (CST) behaviour. Recently, Mawkhlieng and Majumdar [10] reported that presence of bi-dispersed particles having significant size difference causes formation of voids around the larger particles in the STF system. Therefore, the overall contact between particles is reduced, resulting in reduction in peak viscosity and a CST phenomenon prevails. Therefore, a weak contact network structure is formed in such cases. In this study, the SEM micrographs and DLS results clearly show that the synthesised silica particles are polydisperse in nature. Among these three particles, polydispersity is the highest for silica C and the lowest for silica A. Hence, silica C based STF shows CST phenomenon whereas silica A and B based STFs exhibit DST phenomenon owing to lower polydispersity. Notably, in DST, strong contact network structure is formed due to presence of less voids in the network structure. Figure 7 depicts a schematic representation of the effect of polydispersity of particles in hydrocluster formation. In addition, there is more than an order of magnitude difference in peak viscosities between STFs prepared from the smallest (silica A) and the largest particles (silica C).

Critical shear rate and peak viscosity values for all the STFs are summarised in Table 3. The highest peak viscosity and highest critical shear rate are observed in STF A which
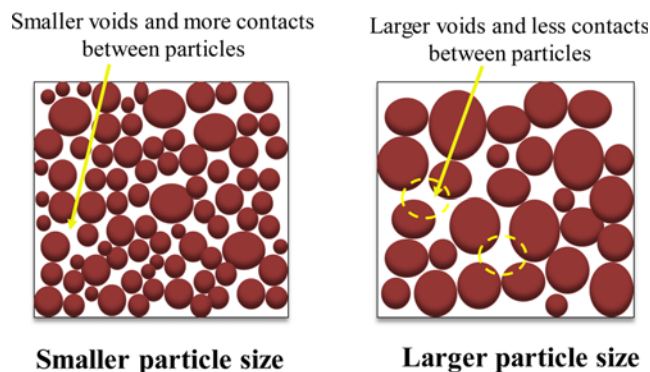

Figure 6. Flow curves of different STFs.

Figure 7. Effect of polydispersity of particles on hydrocluster formation.

Table 3. Rheological parameters of different STFs

STF	Critical shear rate (s^{-1})	Peak viscosity (Pa·s)
STF A	173	88.6
STF B	24.4	62.2
STF C	17.1	4.16

consists of the smallest particles (143 nm). In case of smaller particle size and lower polydispersity, a greater number of particles present in the constant volume of the STF system leads to enhanced inter-particle interactions. Thus, extremely stable hydroclusters are formed which enhance the peak viscosity significantly. Also, smaller particle size translates into higher surface area which creates strong repulsive force among the particles which necessitates more external shear force for actuating the hydrodynamic force. This necessitates higher critical shear rate. Moreover, STF B exhibits lower critical shear rate and lower peak viscosity in comparison with STF A. This is attributed to the fact that with increase in particle size, Brownian motion of the particles is subdued. Therefore, critical shear rate and peak viscosity are found to decrease. This finding is in agreement with other published research work [18].

Surface Morphology of STF Impregnated Kevlar Fabrics

Figure 8 depicts surface morphology of neat and STF impregnated Kevlar fabrics. A thin layer of hydrophobic finish of PTFE coating is present over the neat Kevlar fabric (Figure 8(a)). Figures 8(b), (c) and (d) depict the presence of STF A, B and C over the fabric surface. Notably, most of the STF is filled in the inter-filament gaps within the multifilament yarns of the fabrics. In a previous publication by authors [26], it is reported that distribution of STF over the fabric surface plays a crucial role in determining the impact energy absorption. Greater deposition of STFs in inter-filament gaps of impregnated fabric results in higher impact energy absorption as compared to that in case of superficial deposition of STF over fabric.

Impact Resistance Performance of Neat and STF Impregnated Kevlar Fabrics

Table 4 summarises the results of impact testing of neat (N-K) and STF impregnated (STF A-K, STF B-K and STF C-K) Kevlar fabrics. Add-on (%) of STFs A, B and C in impregnated fabrics is 15.5, 15.8 and 14.2 %, respectively. This indicates an almost similar add-on of STFs, independent of particle size. It is observed from Table 4 that STF impregnated fabrics exhibit higher peak energy and total energy absorption as compared to neat fabric. Generally,
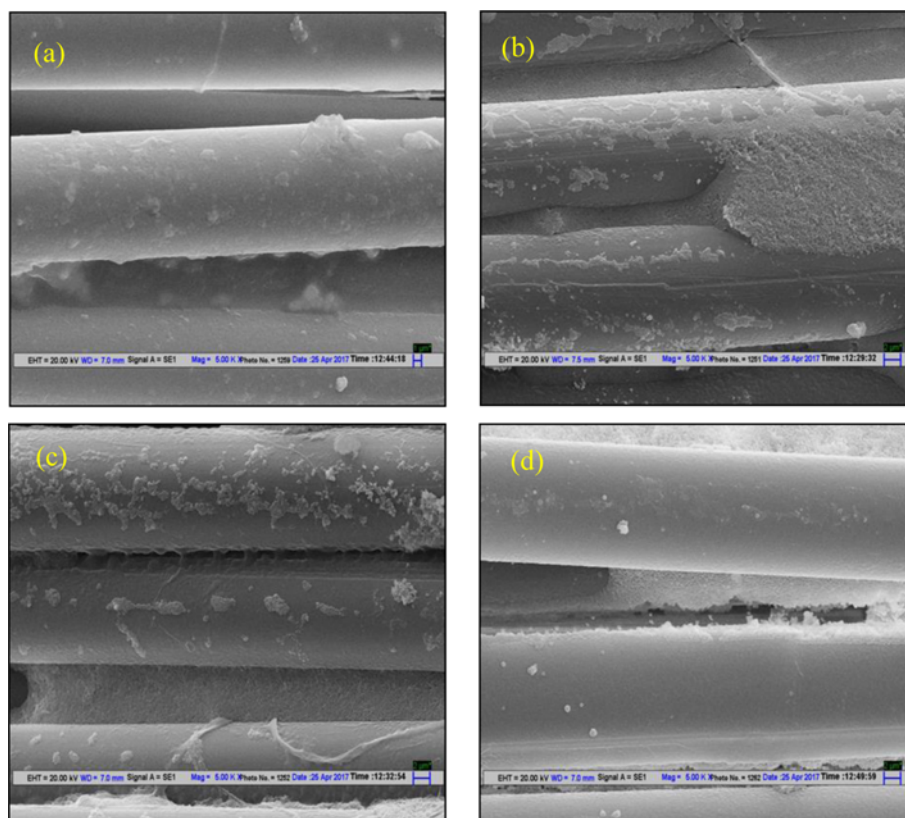

Figure 8. Surface morphology of Kevlar fabrics in (a) neat form; (b) STF A, (c) STF B, and (d) STF C impregnated forms.

Table 4. Impact resistance performance of neat and STF impregnated Kevlar fabrics

Sample code	STF	Add-on (%)	Peak energy absorption (J)	Absolute total energy absorption (J)	Normalised total energy absorption (J)
N-K	-	-	8.4	24.1	24.1
STF A-K	STF A	15.5	63.3	82.8	71.7
STF B-K	STF B	15.8	55.0	72.3	62.4
STF C-K	STF C	14.2	53.3	67.5	59.1

STF is majorly distributed in the interstices of yarns of impregnated fabrics (Figure 8). As the indenter hits the fabric, relative movement between primary and secondary yarns causes shear in STF, resulting in actuation of thickening phenomenon and bonding of primary and secondary yarns [34]. Thus, the stress is distributed over a wider area of the impacted fabric, resulting in increase in energy absorption.

It is also seen from Table 4 that impact resistance performance of STF impregnated fabrics improves with decreasing size of silica particles in STF. STF A-K exhibits the highest peak and total energy absorption of 63.3 and 82.8 J, respectively. This reveals significant increase of 654 and 244 % in peak and total energy absorption of STF A-K in comparison to N-K. This is true even after normalisation with add-on, i.e. even the normalised total energy absorption by STF A-K is 20 % higher than that by N-K. This finding is commensurate with other reported findings [22,35] describing increase in impact energy absorption with increasing peak viscosity of the STF that is impregnated in fabric. Notably, higher the (peak) viscosity achieved by the STF, more the contribution towards energy absorption. Thus, it can be inferred that the shear thickening property of an STF plays dominant role in enhancing the impact energy absorption of high-performance fabrics.

Figures 9(a) and (b) depict force *vs* time and energy *vs* time curves for neat and different STF impregnated fabrics. The change in the impact response of Kevlar fabric after STF impregnation is clearly visible in Figure 9(a). The build-up of force by the fabrics, upon impact, increases almost linearly up to a time of 7 ms. The slope of the curves for all the fabrics is almost similar until this time. This results in development of almost 1086 N force, which is the peak force sustained by N-K. The size of the indenter (13 mm diameter) ensures that upon impact, it engages two to three yarns (*primary yarns*) each in both warp and weft directions. For N-K, these yarns resist the impact till a time of 7 ms or up to the development of 1086 N force. These yarns are no longer able to resist the impact upon reaching the peak force. This results in the yielding of the fabric structure which is manifested as the slippage of the yarns engaged by the impactor and perforation of the fabric as indicated by Figure 9(a). This happens as the clamping force is not sufficiently high to arrest the slippage of the primary yarns at the clamping boundary. Since the yarns remain
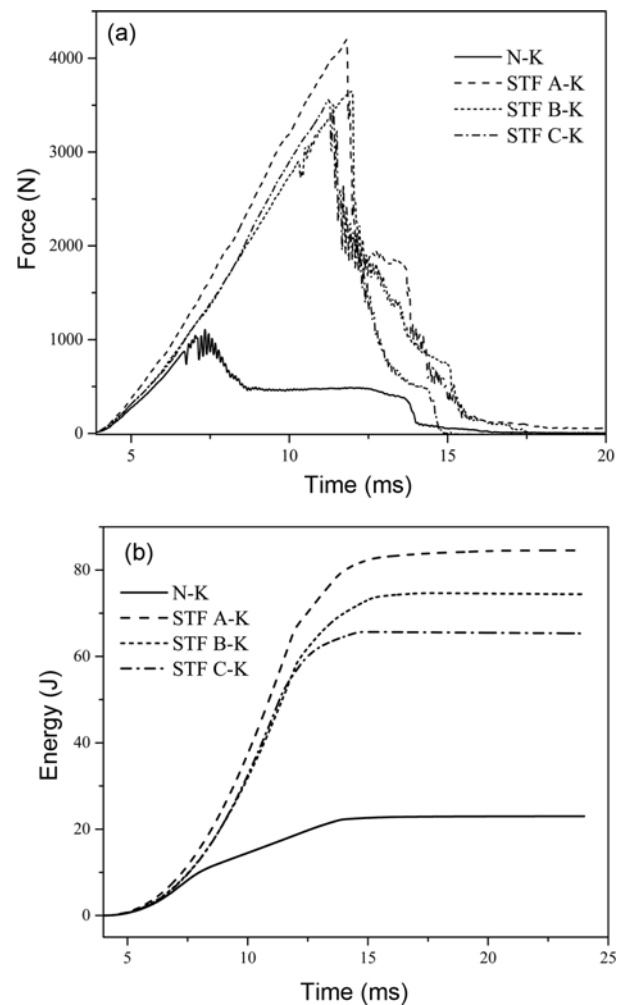
Figure 9. (a) Force *vs* time and (b) energy *vs* time graphs of neat and STF impregnated fabrics.

engaged by the indenter, they keep resisting the indenter, which is visible as gradual and not a sudden decrease in the force build up (Figure 9(a)). In terms of time, the slippage starts at around 7 ms after the impact and continues till 15 ms, i.e. for a duration of ~8 ms. Since the primary yarns continue to resist the movement of indenter in a direction perpendicular to the fabric plane, it keeps absorbing more energy. Also, as the fabric has a woven structure, the
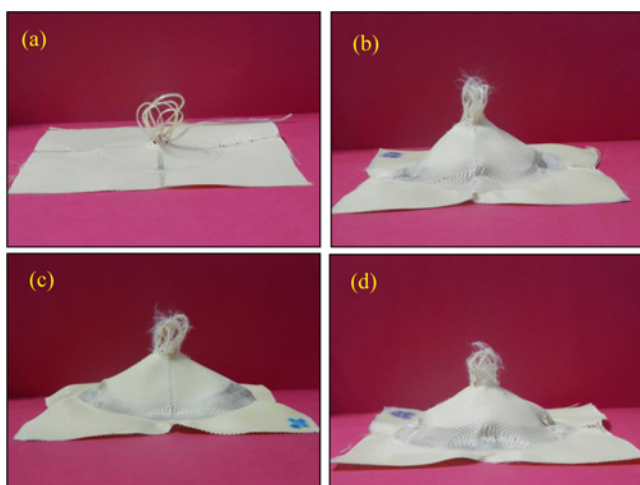
Figure 10. Post impact images of (a) N-K, (b) STF A-K, (c) STF B-K, and (d) STF C-K.

movement of the primary yarns through the interlacements results in a typical *slip-stick phenomenon*, visible in case of N-K [36]. However, this has little practical significance as the fabric failure has already taken place at around 7 ms by perforation. In Figure 9(b), this slippage of yarns manifests itself as a decrease in the slope of the time *vs* energy curve for N-K at ~7 ms (after the peak force is achieved). Hence it can be suggested that for all practical purposes, the real indicator of the true performance of a high-performance material should be the peak energy and not the total energy. Since only the primary yarns of the fabric participate in energy absorption, the rest of the fabric remains unaffected, which is clearly visible in the post-impact image (Figure 10) of N-K. The flat nature of the fabric and the loops formed by the slipped primary yarns can be seen in Figure 10(a).

On the other hand, in case of various STF impregnated fabrics (Figure 9(a)), the force continues to build up with time up to a much longer duration (~13 ms) which results in a much higher build-up of force as compared to that in N-K. Since force continues to build up with time, it also results in absorption of energy at a higher rate than N-K. The slope of the energy *vs* time curves (Figure 9(a)) supports this. The slope for all the fabrics is similar till up to ~7 ms. However, after 7 ms, except for N-K, the slopes for all the STF impregnated fabrics (STF A-K, STF B-K and STF C-K) increase exponentially. This happens as after 7 ms, the secondary yarns start contributing in STF impregnated fabrics whereas perforation takes place in neat fabric. It is also observed that STF impregnated fabrics exhibit catastrophic failure after they attain the peak force (~12-13 ms), primarily as the primary yarn rupture takes place. However, for STF impregnated fabrics, in addition to primary yarns, secondary yarns are also involved in the energy absorption process. This is evident from the post-impact photographs

(Figure 10(b), (c) and (d)) of STF impregnated fabrics which show a distinct dome-like structure. Also, there is no slippage of primary yarns; rather a failure or breakage of primary yarns is clearly visible from photographs. As discussed earlier, upon impact, the sliding of adjacent yarns and filaments provides high shear to the STF lying in their interstices which causes sudden rise in its viscosity (or shear thickening). Additionally, STF also acts a matrix and restricts the slippage of yarns. Both these events contribute to impact energy absorption [37]. Hence, peak viscosity of an STF is decisive factor for enhancement in impact resistance performance of high-performance fabrics.

Conclusion

The effect of differently sized polydisperse silica particles on the rheology of STF and impact resistance of STF impregnated Kevlar fabrics have been investigated. Three polydisperse silica particles of average diameters of 143, 244 and 409 nm, respectively, were synthesised by the Stöber method. The particle size of silica and its size distribution significantly influence the rheological behaviour of STFs. The increasing polydispersity alters the shear thickening behaviour from discontinuous to continuous. STF consisting of the smallest and uniform silica particles exhibit the highest peak viscosity due to increased inter-particle interactions. Further, the rheological performance of different STFs positively correlates to the corresponding impact resistance of Kevlar fabrics impregnated with these STFs. This leads to an important understanding about the role of particle size and its distribution on the rheological behaviour of STF and ensuing impact resistance of Kevlar fabrics treated with STFs.

Acknowledgement

References

1. M. Gameiro, A. Singh, L. Kondic, K. Mischaikow, and J. F. Morris, *Phys. Rev. Fluids*, **5**, 034307 (2020).
2. S. Gürgen and M. A. Sofuoğlu, *J. Manuf. Process,* **56**, 1146 (2020).
3. S. Gürgen and M. A. Sofuoğlu, *Compos. Struct.*, **226**, 111236 (2019).
4. S. Gürgen and M. A. Sofuoğlu, *Compos. Part B Eng.,* **186**, 107831 (2020).
5. S. Gürgen and A. Sert, *Compos. Part B Eng.,* **175**, 107127 (2019).
6. Y. S. Lee, E. D. Wetzel, and N. J. Wagner, *J. Mater. Sci.,* **38**, 2825 (2003).

7. T.-T. Li, W. Dai, L. Wu, H.-K. Peng, X. Zhang, B.-C. Shiu, J.-H. Lin, and C.-W. Lou, *Fiber. Polym.*, **20**, 328 (2019).

8. X. Zhang, T.-T. Li, H.-K. Peng, Z. Wang, J. Huo, C.-W. Lou, and J.-H. Lin, *Fiber. Polym.*, **21**, 1515 (2020).

9. U. Mawkhlieng, A. Majumdar, and D. Bhattacharjee, *Fiber. Polym.*, **22**, 213 (2021).

10. U. Mawkhlieng and A. Majumdar, *Compos. Part B Eng.*, **175**, 107167 (2019).

11. A. Ghosh, A. Majumdar, and B. S. Butola, *Thin-Walled Struct.*, **155**, 106954 (2020).

12. R. Bai, Y. Ma, Z. Lei, Y. Feng, and C. Liu, *Compos. Part B Eng.*, **174**, 106901 (2019).

13. M. Hasanzadeh, V. Mottaghitalab, M. Rezaei, and H. Babaei, *Thin-Walled Struct.*, **119**, 700 (2017).

14. S. Gürgen, M. C. Kuşhan, and W. Li, *Prog. Polym. Sci.*, **75**, 48 (2017).

15. Y.-F. Lee, Y. Luo, S. C. Brown, and N. J. Wagner, *J. Rheol.* **64**, 267 (2020).

16. H. A. Barnes, *J. Rheol.*, **33**, 329 (1989).

17. B.-W. Lee, I.-J. Kim, and C.-G. Kim, *J. Compos. Mater.*, **43**, 2679 (2009).

18. S. Li, J. Wang, S. Zhao, W. Cai, Z. Wang, and S. Wang, *J. Mater. Sci. Technol.*, **33**, 261 (2017).

19. N. Asija, H. Chouhan, and N. Bhatnagar, *ISME J. Manuf. Sci.*, **6**, 9 (2017).

20. I. Wagstaff and C. E. Chaffey, *J. Colloid Interface Sci.*, **59**, 53 (1977).

21. M. Bajya, A. Majumdar, B. S. Butola, S. K. Verma, and D. Bhattacharjee, *Compos. Part B Eng.*, **183**, 107721 (2020).

22. L. Liu, Z. Yang, Z. Zhao, X. Liu, and W. Chen, *Thin-Walled Struct.*, **151**, 106717 (2020).

23. K. Fu, H. Wang, Y. X. Zhang, L. Ye, J. P. Escobedo, P. J. Hazell, K. Friedrich, and S. Dai, *Int. J. Impact Eng.*, **139**, 103525 (2020).

24. Y. Park, Y. Kim, A. H. Baluch, and C.-G. Kim, *Int. J. Impact Eng.*, **72**, 67 (2014).

25. X. D. Wang, Z. X. Shen, T. Sang, X. Bin Cheng, M. F. Li, L. Y. Chen, and Z. S. Wang, *J. Colloid Interface Sci.*, **341**, 23 (2010).

26. K. Talreja, I. Chauhan, A. Ghosh, A. Majumdar, and B. S. Butola, *RSC Adv.*, **7**, 49787 (2017).

27. P. E. Imoisili, K. O. Ukoba, and T. C. Jen, *J. Mater. Res. Technol.*, **9**, 307 (2020).

28. M. A. Bourebrab, D. T. Oben, G. G. Durand, P. G. Taylor, J. I. Bruce, A. R. Bassindale, and A. Taylor, *J. Sol-Gel Sci. Technol.*, **88**, 430 (2018).

29. M. Kaszuba, D. McKnight, M. T. Connah, F. K. McNeil-Watson, and U. Nobbmann, *J. Nanoparticle Res.*, **10**, 823 (2007).

30. H. Udono, K. Uruga, T. Tsukada, and M. Sakai, *Powder Technol.*, **361**, 203 (2020).

31. F. J. Galindo-Rosales and F. J. Rubio-Hernández in "Numerical Simulations - Examples and Applications in Computational Fluid Dynamics" (L. Angermann Ed.), IntechOpen, Rijeka, Croatia, https://www.intechopen.com/chapters/12611, pp.3-22, 2010.

32. S. Gürgen and R. J. A. de Sousa, *Arch. Civ. Mech. Eng.,* **20**, 1 (2020).

33. S. Gürgen, *J. Nano Res.*, **56**, 63 (2019).

34. S. Arora, A. Majumdar, and B. S. Butola, *Compos. Struct.*, **233**, 111720 (2020).

35. M. Wei, L. Sun, and J. Zhu, *Mater. Des.*, **196**, 109078 (2020).

36. A. Majumdar, B. S. Butola, and A. Srivastava, *Mater. Des.*, **51**, 148 (2013).

37. P. Dixit, A. Ghosh, and A. Majumdar, *J. Mater. Sci.*, **54**, 13106 (2019).